Charge Calibration for the Test Beam Characterisation of an APTS Prototype

Judith Schlaadt, Johannes Gutenberg University Mainz, Germany

September 7, 2022

Supervisors: Dr. Finn Feindt, Gianpiero Vignola

Abstract

Silicon detectors with specific requirements considering the position and time resolution, as well as the material budget and rate capability, are needed for different applications in beam telescopes and linear e^+e^- collider experiments. In collaboration with CERN, the Tangerine project focuses on the development of such a device and currently studies several samples with different layouts. This report addresses the charge calibration of one of these prototypes, namely APTS sample 24, which was done by performing x-ray fluorescence measurements with different target materials. After implementing the obtained calibration factors for the 16 pixels of the device under test in the data acquisition software, it was used to analyse test beam data. Comparing the data before and after the calibration showed that implementing such a factor influences several parameters and results in an improved position resolution.

Contents

1 The Tangerine Project

The Tangerine project (**T**ow**A**rds **N**ext **GE**ne**R**ation SI**I**lico**N** D**E**tectors) started in September 2020 as a part of the ATLAS collaboration at DESY. Its main goal is to design a monolithic active pixel sensor which fulfils the following requirements:

- Position resolution of approximately 3 µm
- Time resolution of 1 - 10 ns
- Low material budget of 50 µm silicon
- Rate capabilities of 1 MHz particle rate
- In-pixel charge measurement via ToT (time over threshold)

The main application for such a device is the usage in beam telescopes. Another possible application would be in linear e^+e^- collider experiments. Currently, three layouts (standard, n-blanket and n-gap) for the design of the sensitive volume of the pixels are under study. A scheme of the so-called n-blanket layout, which I used for my project, is shown in figure 1. Independent of the used layout, an incoming particle generates electron-hole pairs in the sensitive volume of the pixel. These charge carriers start to drift due to an external voltage applied to the collection electrode and the p-doped substrate. The electrons induce a signal in the collection electrode while drifting towards it. This signal is read out by electronic components implemented in a p-doped well (pink area in the scheme). Due to this well, the readout electronics are shielded from the electric field. Compared to the standard one, the n-blanket layout has an additional n-doped layer (shown in light green) which extends the electric field in the sensitive volume. Due to this, more charge carriers get collected and the time resolution is improved [1].

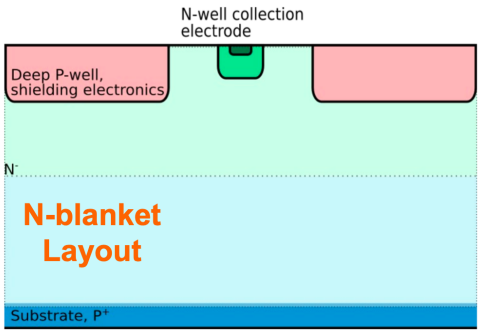

Figure 1: N-blanket layout for the sensitive volume of a pixel. An external voltage is applied to the n-well collection electrode (dark green) and the p-doped substrate (dark blue). The name of the design refers to the additional n-doped layer (light green), which extends the electric field compared to the standard layout. The readout electronics are implemented in the pixel and shielded from the electric field by a p-doped well (pink) [1].

To optimise the pixel design, an extensive program of simulations as well as test beam measurements with different samples are performed. Thereby, the prototypes consist of 16 pixels arranged as four pixels per row and column with different pixel pitches. The simulations can be validated by analysing the test beam data. But to do so, a calibration factor is required for every pixel to convert the pixel charge, which was measured in arbitrary units to units of energy.
During my project, I determined the calibration factors for the 16 pixels of APTS sample 24 via x-ray fluorescence spectroscopy, see section 2. After implementing this factor in the data acquisition software, I also analysed the differences in seed charge and position resolution for this prototype before and after the calibration, as described in section 3. In the final section (section 4), the main results of the measurements will be summarised, and an outlook on possible further measurements will be given.

2 Pixel Calibration

2.1 X-Ray Fluorescence Spectroscopy

In order to perform x-ray fluorescence spectroscopy, an x-ray tube in combination with a target material is required. The schematic working principle of an x-ray tube is shown in figure 2.

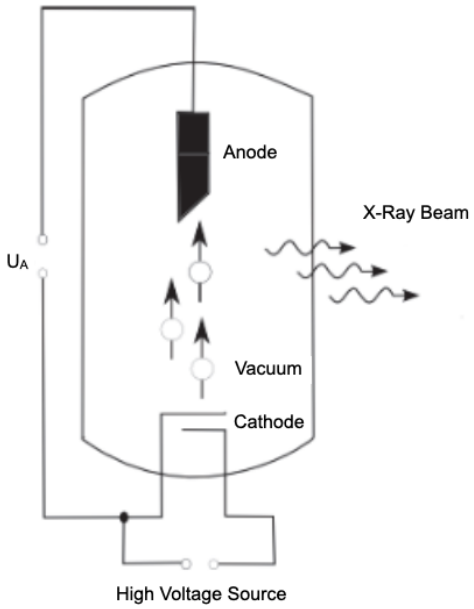

Figure 2: Schematic principle of an x-ray tube. A thermionic cathode is heated in vacuum to emit electrons, which are then accelerated towards the anode by the tube voltage U_A. When the electrons collide with the anode, they get decelerated and emit continuous bremsstrahlung with characteristic x-rays, which are visible as sharp peaks in the spectrum [2].

A cathode is heated inside an evacuated glass tube by applying a high voltage. This causes the thermionic emission of electrons which are then accelerated towards the anode by the tube voltage U_A. The electrons get decelerated when they collide with the anode and therefore emit bremsstrahlung. The corresponding spectrum is continuous but also shows sharp peaks. These are called characteristic x-rays and depend on the used anode material, which in this case was tungsten. The x-rays, which are emitted under an angle of 90°, then hit the target material [2]. In general, the interaction of photons with matter can be described by three different effects, namely pair creation, Compton scattering and the photoelectric effect. The latter is the dominant effect for x-rays with an energy less than 100 keV. In this setup, the maximum x-ray energy is 35 keV, since the tube voltage is limited to $U_A = 35\,\text{kV}$. Figure 3 shows a scheme of the expected photoelectric effect, which leads to the emission of fluorescent x-rays [2]. Thereby, the incident radiation gets absorbed by atomic electrons of the target material, which increases their energy. If the energy of the x-rays E_γ is higher than the binding energy of the electron E_b, the latter is ejected from the atom with a kinetic energy of

$$E_{kin} = E_\gamma - E_b \quad [3].$$

The K-shell electrons are most likely to be ejected as photo-electrons, whereby they leave a vacant position in the corresponding energy level. An electron of a higher energy shell then emits fluorescent x-rays to fill this vacancy [3]. The main transitions which can occur are K_α or K_β transitions, whereby an L-shell electron or an M-shell electron respectively emit x-rays to fill the vacancy in the K-shell. But due to the fine structure splitting of atomic energy levels, transitions are also possible between different fine structure levels depending on quantum-mechanical selection rules.

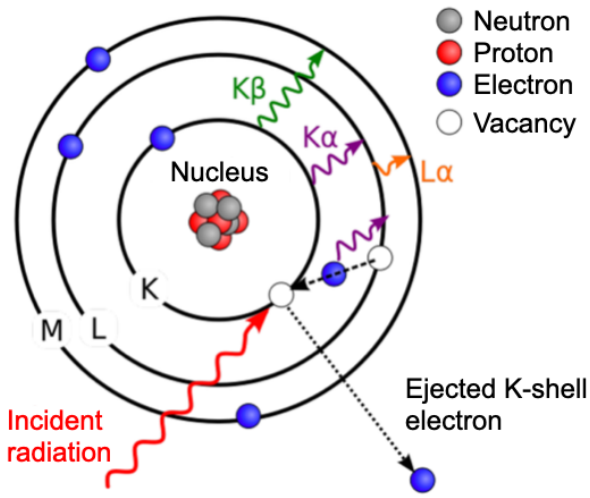

Figure 3: Schematic principle of x-ray fluorescence [2]. The incident radiation gets absorbed by an atomic electron. If the x-ray energy is sufficiently high, the electron gets ejected from the K-shell and generates a vacant position. An electron of a higher energy shell (f.e. the L- or M-shell) then emits fluorescent x-rays to fill this vacancy [3].

K_{α_1} or K_{α_2} transitions for example refer to transitions from the L_3 energy level or the L_2 energy level respectively to the K-shell. The transition energies and hence the energy of the emitted fluorescent x-rays are characteristic for different elements. Therefore, they can be used for calibration purposes as well as for the identification of elements [2].

2.2 Experimental Setup and Measurement

In order to perform the x-ray fluorescence measurements, a setup of the University of Hamburg (UHH) was used, as can be seen in figure 4. The left picture shows the whole experimental setup, including the x-ray tube in the upper left part of the box. The picture was taken while the cathode was used, which is why it is glowing. The emitted x-rays then hit the target material (see right picture), which was titanium and copper respectively. Below the target, the so-called chip board with APTS sample 24 was placed. This device under test (DUT) has an n-blanket layout with 25 µm pitch. The chip board is part of the Caribou data acquisition system and is connected to the Control and Readout (CaR) board, which among other things, controls the bias voltages of the sample. For these measurements, the bias voltages of the p-doped well and substrate were set to $-3.6\,\mathrm{V}$. The board is also used to read out the pixel signals and is connected to the FPGA board, which is taped to the wall of the box. Thereby, the Field-Programmable Gate Array (FPGA) on this board is used to perform different logic functions [4].

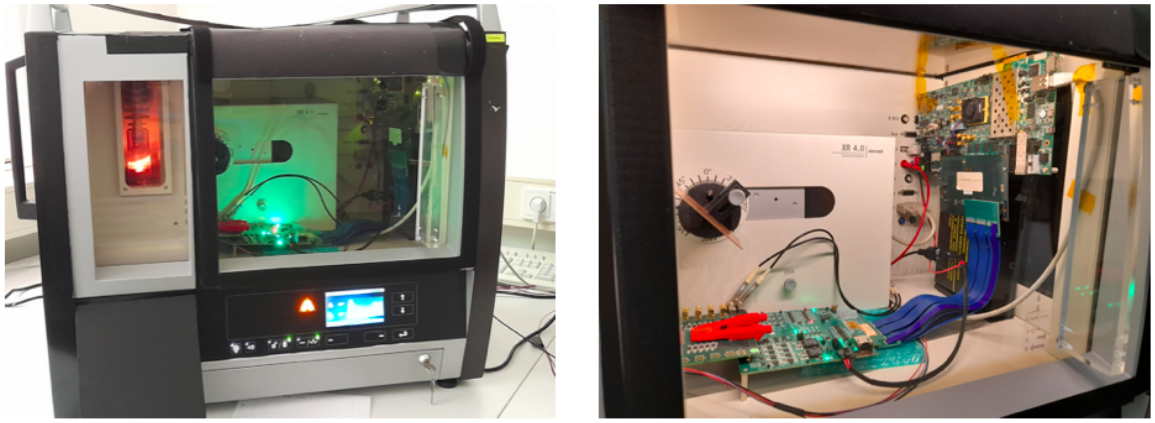

Figure 4: Experimental setup for the x-ray fluorescence measurements. The x-ray tube can be seen in the upper left, while the target material, which is attached to a rotatable arm, is in the right part of the box. Below the target, a chip board with APTS sample 24 was placed. The chip board, as well as the CaR board and the FPGA board, are part of the Caribou data acquisition system [4].

For the data acquisition, the software EUDAQ2 was used. This software checks if signals of the different pixels i are above the set threshold. If this is the case, it also analyses the measured waveforms and determines the amplitude of the signal as the difference between the maximum and the minimum of the signal voltage $A[i] = \max[i] - \min[i]$. In

the next step, histograms for the cluster charge were generated by plotting the number of entries versus the signal amplitudes $A[i]$ in arbitrary units. This is due to the fact that the voltage is proportional to the charge of a signal, but the conversion factor is unknown in this case.

2.3 Data Analysis

The aim of this analysis is to determine a calibration factor for the signal amplitudes, which allows the conversion of the pixel charge in arbitrary units into the energy of the generated charge carriers. To do so, the peaks in the measured spectra have to be identified, and their centre position has to be determined, which for known transition energies allows the calculation of a calibration factor.

2.3.1 Titanium

The measured spectra for the titanium target show two peaks for every pixel. These correspond to the K_α and K_β transition since the transitions between different fine structure levels could not be resolved with this setup. Therefore, the mean value of K_{α_1} and K_{α_2} was used to determine the transition energy $K_\alpha = (4.507 \pm 0.003)$ keV [5]. The same applies to the fine structure transitions from the M-shell to the K-shell, which is why the mean value $K_\beta = (4.943 \pm 0.011)$ keV was used for the calibration [5]. For the 16 pixels of the used sample, the same procedure was performed to analyse the data, but in the following will only be shown exemplarily for pixel 3_1.

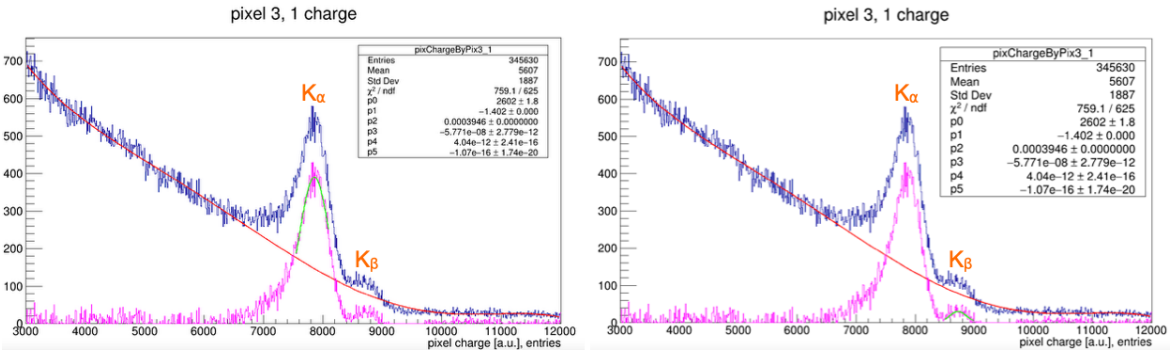

Figure 5: Measured spectra of pixel 3_1 for the titanium target. The original spectrum is shown in blue with the labelled peaks for the K_α and K_β transition. The red curve is the extrapolated fit of the background. Subtracting it from the spectrum results in the pink curve. The left plot shows the Gaussian fit of the K_α peak in green, while the right plot does the same for the K_β peak.

A fit with a 5th degree polynomial of the form $f(x) = p_0 + p_1 \cdot x + p_2 \cdot x^2 + p_3 \cdot x^3 + p_4 \cdot x^4 + p_5 \cdot x^5$ was performed to describe the background for the part of the titanium spectrum, which is shown in blue in figure 5. Thereby, the fit range excluded both peaks. The results of the fit parameters p_0 - p_5 are shown in the legends of the plots and were used afterwards

to extrapolate the fit (red curve). The subtraction of the background from the spectrum results in the pink curve. Since the position of the centre of the peaks is required for the calibration, a Gaussian fit of each peak was performed. For this, the expression $f(x) = c \cdot e^{-\frac{(x-\bar{x})^2}{2\sigma^2}}$ was used, whereby c refers to the maximal amplitude of the peak, $\bar{x}$ to the position of the centre of the peak, and σ to the standard deviation. The Gaussian fits are shown in green in figure 5. Thereby, the left plot shows the fit of the peak corresponding to the K_α transition, while the right plot shows the same for the K_β transition peak. To improve the quality of the fit, the fit range was varied. Especially for the K_α transition peak, the value for χ^2 over the number of degrees of freedom (χ^2 / NDF) was significantly reduced by excluding the tail on the left part of the peak. Since this peak also superimposes the K_β transition peak, the χ^2 / NDF value of the latter is not as small as the one for the K_α transition. The corresponding fit results are listed in table 1.

Table 1: Results of the Gaussian fits of the peaks corresponding to the K_α and K_β transition in the titanium spectrum of pixel 3_1.

Pixel 3_1	K_α transition	K_β transition
Amplitude c	390 ± 4	30 ± 1
Mean value $\bar{x}$	7859 ± 4	8725 ± 11
Standard deviation σ	253 ± 5	143 ± 16
χ^2 / NDF	76.9 / 52	108.4 / 27

2.3.2 Copper

The spectra for copper only show a single peak, which corresponds to the K_α transition. The mean value of the fine structure transitions for this case is $K_\alpha = (8.038 \pm 0.010)$ keV [5]. However, some pixels already started to saturate at this energy, which is why the peak was only partially visible in these cases.

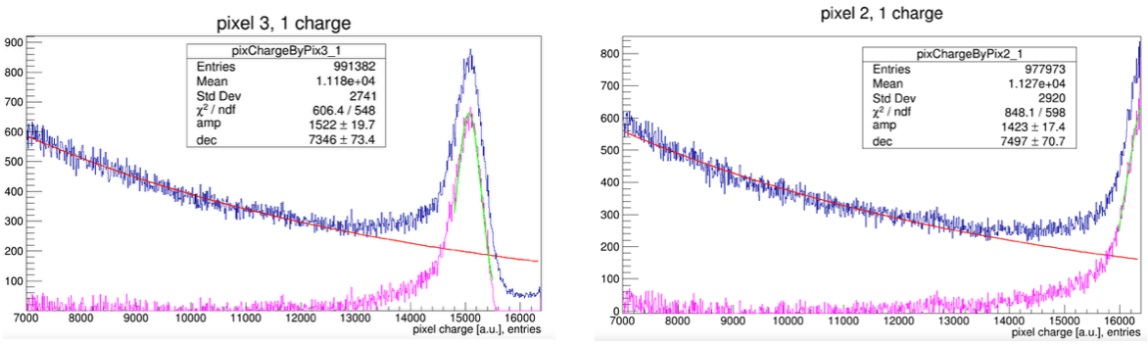

Figure 6: Measured spectra of pixel 3_1 and pixel 2_1 for the copper target. The original spectrum is shown in blue, whereby the peak of the K_α transition is only partially visible for the right plot. Subtracting the extrapolated fit of the background (red curve) from the spectrum results in the pink curve. Afterwards, a Gaussian fit of the peak was performed (green curve).

In figure 6, the spectrum (blue curve) of Pixel 3_1 on the left is compared to the spectrum of Pixel 2_1 on the right. For the latter, only a fraction of the expected peak is visible. Due to this, the fit range for the background was limited to energies below the peak. After performing this fit with a 5th-degree polynomial and extrapolating it to the peak area, it became apparent that the background was not well described in this case. Therefore, an exponential function of the form $f(x) = amp \cdot e^{-dec \cdot x}$ was used for the fit instead (red curve). This improved the quality of the fit, but was still not ideal, as can be seen in the left plot. There the blue and the right curve do not match at higher energies. The results for the amplitude *amp* and the parameter *dec* are listed in the legends of the plots. The pink curve shows again the spectrum when the background is subtracted. Performing a Gaussian fit of the peak (green curve) resulted in the parameters given in table 2. For pixels like pixel 3_1 where the peak was completely visible, the χ^2 / NDF value improved by excluding the tail on the left side of the peak. For pixels where the peak was only partially visible (like for pixel 2_1), the fit parameters are associated with higher uncertainty. Due to this, the peak position for the copper spectra was not determined as precisely as for the titanium spectra.

Table 2: Results of the Gaussian fit of the peak corresponding to the K_α transition in the copper spectrum of pixel 3_1 and pixel 2_1.

K_α transition	Pixel 3_1	Pixel 2_1
Amplitude c	661 ± 5	694 ± 54
Mean value $\bar{x}$	15066 ± 3	16538 ± 72
Standard deviation σ	222 ± 2	393 ± 39
χ^2 / NDF	57.3 / 52	55.5 / 37

2.3.3 Calibration Factor

In order to obtain the calibration factor for the cluster charge, the transition energy was plotted versus the position of the centre of the corresponding peak, as can be seen in figure 7 for pixel 3_1. Thereby, the error bars of the data points were too small to be visible, which is why the diamond shape was used to mark them. Afterwards a linear fit of the form $f(x) = m \cdot x + b$ with slope m and intercept b was performed. Since several pixels already saturated at the position of the copper peak, only the data points of the titanium measurement were taken into account for this fit. Extrapolating the fit to the K_α transition energy of copper (dotted orange line) shows a discrepancy between the expected and the real position of the corresponding peak. This might be due to non-linearities in the gain of the pixel, which were not further analysed in this project.

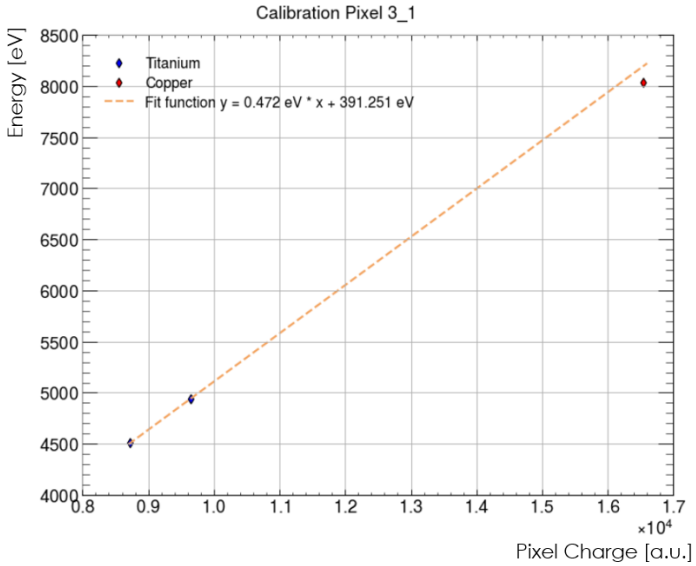

Figure 7: Plot of the transition energy versus the corresponding peak position. A linear fit (orange line) was performed for the titanium data points (shown in blue) and extrapolated towards the position of the copper data point (red marker).

After performing this fit for every pixel i, the fit results for m and b were implemented in EUDAQ2 to obtain the calibrated signal amplitude $A_{cal}[i] = m[i] \cdot (\max[i] - \min[i]) + b[i]$. The calibrated spectrum of pixel 3_1 for titanium can be seen in figure 8 on the left and the one for copper on the right. For titanium, the peaks are positioned at the expected energy values. But as already pointed out, there is a small discrepancy for the copper peak.

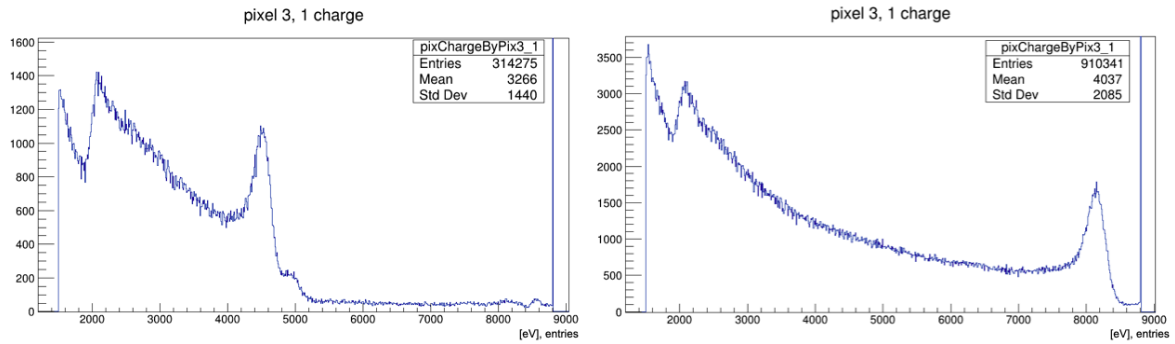

Figure 8: Calibrated spectra of pixel 3_1 for the measurements with titanium (left plot) and copper (right plot).

2.4 Discussion of the Results

A calibration factor for every pixel of APTS sample 24 was determined by using the measurements with the titanium target. These factors were then successfully imple-

mented in the data acquisition software EUDAQ2 and can be used for the test beam characterisation of this prototype.

There are several possible sources of uncertainties caused by the data analysis. For the titanium measurement, the fit range of the peaks had to be reduced to improve the χ^2 / NDF value. This procedure worked quite well when the tail on the left side of the K_α peak was excluded. For the K_β peak, on the other hand, the fit parameters were still associated with higher errors compared to the K_α peak since both are partially superimposed. In this case, a fit with the sum of two Gaussian functions might increase the quality of the fit. For the analysis of the measurements with copper, the background fit was performed with an exponential function. This fit describes the part on the left side of the peak well but does not match the spectrum on the right side. Also, other functions (like polynomials of different degrees) failed to describe the background, as the right part of the spectrum was not always visible due to the saturation of pixels. For the same reason, it was not possible to fit these peaks as precisely as the titanium peaks. Therefore, only the latter results were used to determine the calibration factor.
Afterwards, the linear fit for the calibration factor was extrapolated to the position of the copper peak, and a discrepancy between the calculated and the theoretical energy value of the transition was observed. This indicates that fit overestimates the transition energies in this energy range. To verify that this is the case and to improve the fit in general, more data points are required.
A possible metal for further measurements would be nickel since the mean value of the K_{α_1} and K_{α_2} transition is $K_\alpha = (7.470 \pm 0.008)$keV and therefore smaller than the one for copper [5]. In this case, the peaks should be visible for every pixel since they start to saturate at higher energies, namely between approximately 8.1 keV and 9.4 keV.
A measurement with aluminium could also improve the fit quality for the low energy range since the mean transition energy $K_\alpha = 1.487$ keV. This peak will most likely at least partially superimpose the K_β peak since the transition energy for the latter is $K_\beta = (1.559 \pm 0.003)$ keV [5].

3 Test Beam Measurements

3.1 Test Beam Telescope

The data which was used for the following analysis, was already taken by members of the Tangerine project in June 2022 at the test beam facility DESY II. Previous measurements for the calibration of the data acquisition software were performed at the test beam facility MAMI (Mainz Microtron) in collaboration with scientists from CERN. The measurements at DESY were performed with the MIMOSA beam telescope which can be seen in figure 9. It consists of six detector planes, which can be used to reconstruct particle tracks. The DUT, which in this case was APTS sample 24, was placed in the middle of the telescope. It was tested for different electron energies, but only measurements with a beam energy of 4 GeV were used for this analysis [7].

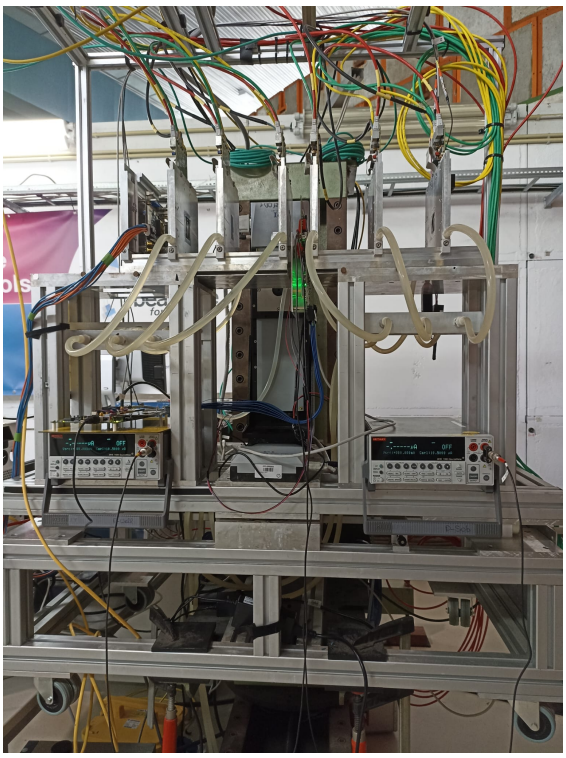

Figure 9: Picture of the beam telescope MIMOSA at the test beam facility DESY II with the device under test (DUT) in the middle. The electron beam traverses the six detector planes of the telescope from the right to the left [7].

The scheme on the right in figure 10 shows the six planes of the MIMOSA beam telescope in red and the DUT in yellow. The electron beam (dotted black line) traverses the setup from the right side to the left and thereby generates signals in the detector layers (red cross) and the DUT (yellow cross). When several adjacent pixels measure a signal, they are called a cluster and are marked in the scheme with a red square.

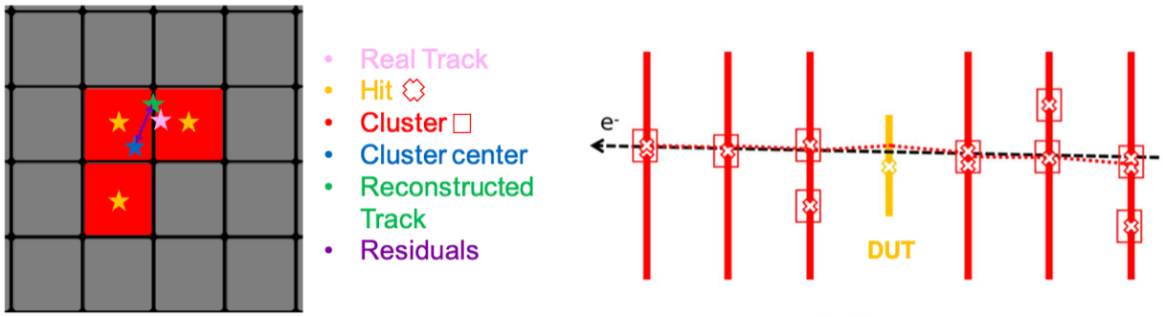

Figure 10: Scheme of the working principle of the beam telescope MIMOSA. The left picture shows the top view of a pixel sensor with four pixels per row and column. The beam telescope in the right picture consists of six detector planes (shown in red) and the DUT (shown in yellow) [8].

The measured hits are then used to reconstruct the particle track (dotted red line). Since the detector planes have a finite thickness, scattering effects are also taken into account. The left scheme in figure 10 shows the top view of a pixel detector. When it gets hit by a beam electron (pink star), the signal amplitude of several adjacent pixels can be above the set threshold, which indicates a hit (yellow star). The corresponding pixels are marked in red and form a cluster, whereby the mean position of the cluster is shown as a blue star. Using the Corryvreckan software to analyse the hit positions of several pixel layers, the particle track can be reconstructed. Considering the reconstructed trajectory, the expected hit position is marked with a green star. The difference between the reconstructed position and the centre of the cluster is called a residual. These residuals indicate the limit of the position resolution of a detector system.
One approach to reduce the standard deviation of the residuals and hence improve the position resolution is to use the weighted cluster position instead of the mean one since it takes the signal amplitudes of the pixels of a cluster into account.

3.2 Data Analysis

The Corryvreckan software is used to analyse test beam data. This software uses different modules to perform the required tasks, like reading in raw data and identifying clusters. To analyse the correlation of clusters of different detectors, the correlation module is used, which creates correlation and timing plots with respect to a reference detector. Another module is used for the tracking of particles, which traverse through the different telescope planes. These planes have to be aligned to improve the reconstruction of different particle tracks, which is done with two additional modules. For the alignments, the x- and y- coordinate of the different detector layers, as well as their rotation angles, can be varied. When the alignment of the telescope planes is done, the DUT also has to be aligned with respect to the beam telescope. Afterwards, several histograms, for example, for the position, size, and charge of associated clusters, as well as local residuals in x- and y-direction, can be generated by using the "AnalysisDUT" module [9].
The alignment of the telescope and the DUT was done for a run with APTS sample 24, during which the same bias voltage of $-3.6\,\mathrm{V}$ were applied. In the following, two parameters, namely the seed charge and the position resolution of the prototype, will be compared before and after the implementation of the calibration factor.

3.2.1 Seed Charge of Associated Clusters

A seed pixel is the pixel in a cluster which measured the highest signal amplitude. The charge distribution of these pixels is expected to follow a Landau distribution and can be seen in figure 11 before (left plot) and after (right plot) the calibration factor was implemented.
The corresponding coefficient of variation, which is defined as the ration of the standard deviation and the mean value of a distribution $\mathrm{CV} = \frac{\sigma}{\bar{x}}$ is given in table 3 [10]. The results indicate that after the calibration, the dispersion of the distribution is reduced.

Due to this, the position resolution is expected to improve since for this, the signal amplitudes of the different pixels of a cluster are taken into account.

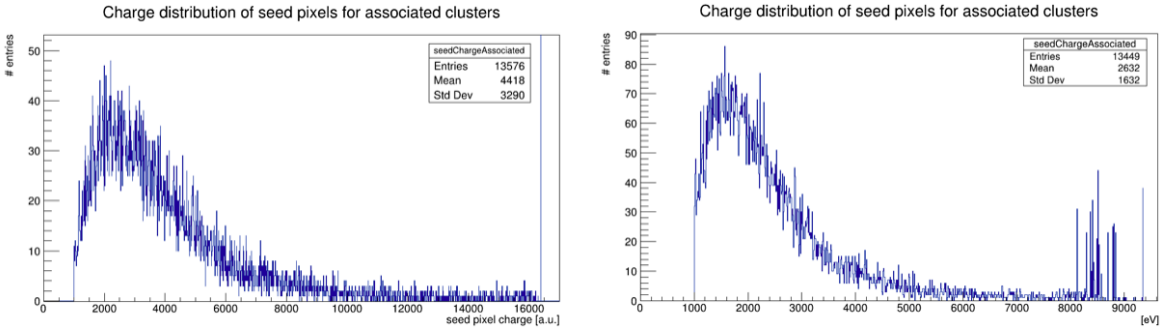

Figure 11: Charge distribution of seed pixels for associated clusters before (left plot) and after the calibration (right plot).

Table 3: Coefficient of variation for the seed charge distributions before and after implementing the calibration factor.

Landau distribution	Coefficient of variation
Before calibration	$3290 \,/\, 4418 \approx 0.745$
After calibration	$1632 \,/\, 2632 \approx 0.620$

3.2.2 Position Resolution

The best position resolution is expected for a cluster size of two adjacent pixels. As already mentioned before, it is limited by the standard deviation of the beam telescope residuals and the DUT residuals. The latter can be reduced by implementing the calibration factor. This can be seen in figure 12, as it compares the residuals for the y-direction before (left plot) and after (right plot) the calibration.

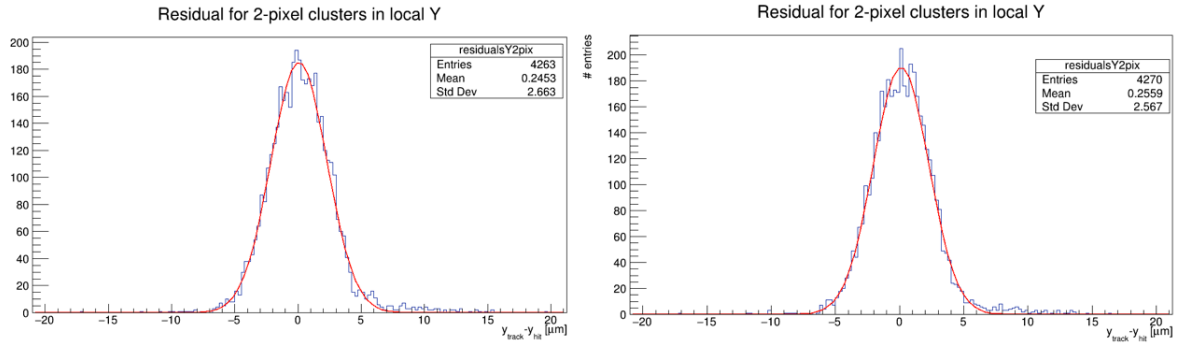

Figure 12: DUT residuals in y-direction for a cluster size of two pixels before (left plot) and after (right plot) implementing the calibration factor. A Gaussian fit (red curve) was performed to obtain the standard deviation of the distribution.

The standard deviation of the residuals in x- and y-direction before and after applying the calibration factor were obtained by performing a Gaussian fit of the form $f(x) = c \cdot e^{-\frac{(x-\bar{x})^2}{2\sigma^2}}$. The results of this fit are listed in table 4. These are preliminary results in the sense that the standard deviation of the residuals can still be improved by refining the Corryvreckan analysis. However, this was not the main objective of this work. The analysis showed that the dispersion of the residuals in y-direction is smaller than the one in x-direction. But in both cases, the standard deviation was reduced after using the calibration factor, which indicates an improved position resolution.

Table 4: Standard deviation of the residuals of the sample in x- and y-direction before and after the calibration for a cluster size of two pixels.

DUT residuals	σ_x [µm]	σ_y [µm]
Before calibration	3.138 ± 0.034	2.218 ± 0.027
After calibration	3.070 ± 0.032	2.168 ± 0.026

3.3 Discussion of the Results

Using test beam data to characterise the sample showed that the implementation of the calibration factor influenced different parameters. But a direct comparison has only been made for the residuals of two-pixel clusters and the seed charge. For the latter, the dispersion of the corresponding Landau distribution was reduced, which is indicated by a reduced coefficient of variation. Also, the standard deviation of the residuals in x- and y-direction for two-pixel clusters was reduced after the calibration, which resulted in an improved position resolution.
Again, there are possible sources of uncertainties caused by the data analysis. First of all, the results of the calibration factors are associated with errors, which cannot be implemented in the data acquisition software. Also, for this analysis, the standard deviation in y-direction is smaller than the one in x-direction. This might indicate that the alignment of the DUT with respect to the beam telescope is not ideal for this direction and could still be improved.

4 Conclusions and Outlook

Within this project, it has been shown that x-ray fluorescence spectroscopy is a suitable tool to determine calibration factors for pixel sensors. It was used to determine the calibration factors for 16 pixels of a specific device under test, namely APTS sample 24, but can also be used for the calibration of other prototypes with different layouts. First comparisons of analysed test beam data before and after the calibration showed that implementing such a factor influences several parameters, like the cluster or seed charge, but also leads to an improved position resolution.
The calibration factors were determined using a linear fit, which can be improved by performing further measurements with different target materials. It would be reasonable

to perform these measurements with aluminium, titanium, and nickel to cover the energy range, which can be measured with the prototypes.
Using the results of this work, it is also possible to directly compare the test beam data to the performed simulations. To do so, the calibrated amplitude of the waveforms only has to be divided by a factor of $E \approx 3.6\,\mathrm{eV}$ (for silicon), which converts the energy of the incident particle into the number of generated electron-hole pairs [11].

5 References

[1] Talk "First test-beam result on MAPS prototypes in 65 nm process". *Gianpiero Vignola* on behalf of the Tangerine Collaboration at 10th Beam Telescopes and Test Beams Workshop (BTTB10), Lecce, June 22nd 2022.

[2] Manual "Anwendung von Röntgenstrahlung in der Detektorphysik". *Prof. Dr. Erika Garutti*. January 15th 2014. https://www.yumpu.com/de/document/read/25333136/anwendung-von-rontgenstrahlung-in-der-detektorphysik.

[3] S. Tavernier. "Experimental Techniques in Nuclear and Particle Physics". First edition, Springer Berlin, Heidelberg, 2010. https://doi.org/10.1007/978-3-642-00829-0.

[4] T. Vanat et al. "Caribou – A versatile data acquisition system". In: *Proceedings of Topical Workshop on Electronics for Particle Physics volume 370* (2020). https://doi.org/10.22323/1.370.0100.

[5] National Institute of Standards and Technology: Standard Reference Database. https://physics.nist.gov/PhysRefData/XrayTrans/Html/search.html. Access date: August 9th 2022.

[6] Royal Society of Chemistry. https://www.rsc.org/periodic-table/. Access date: August 19th 2022.

[7] Talk "Monte Carlo simulations of a beam telescope setup based on the 65 nm CMOS Imaging Technology". *Sara Ruiz Daza* on behalf of the Tangerine Collaboration at 10th Beam Telescopes and Test Beams Workshop (BTTB10), Lecce, June 21st 2022.

[8] G., private communication.

[9] "User Manual for the Corryvreckan Test Beam Data Reconstruction Framework, Version 1.0". *J. Kröger, S. Spannagel, M. Williams*. 2019. https://doi.org/10.48550/arxiv.1912.00856.

[10] European Comission. https://datacollection.jrc.ec.europa.eu/wordef/coefficient-of-variation. Access date: August 19th 2022.

[11] F. Feindt, private communication.

List of Figures

List of Tables